

## RESEARCH ARTICLE

# Heavy-Lift Multirotor Unmanned Aerial Vehicles Characterization and Sizing

DENIS KOTARSKI<sup>1,2</sup>, PETAR PILJEK<sup>2</sup>, AND JOSIP KASAC<sup>2</sup><sup>1</sup>Department of Mechanical Engineering, Karlovac University of Applied Sciences, 47000 Karlovac, Croatia<sup>2</sup>Faculty of Mechanical Engineering and Naval Architecture, University of Zagreb, 10000 Zagreb, Croatia

Corresponding author: Denis Kotarski (denis.kotarski@vuka.hr)

This work was supported by the European Regional Development Fund, Operational Program Competitiveness and Cohesion 2014–2020 under Grant KK.01.1.1.04.0092.

**ABSTRACT** In this paper, the characterization and sizing of heavy-lift multirotor UAVs are carried out. For this purpose, the electric multirotor UAV system is briefly described, and the parameters are carefully selected encompassing a wide range of UAVs regarding size and power. In the first phase, comprehensive experimental measurements are conducted for selected propulsion components. Through a systematic data acquisition process, a database for two series of electric propulsion units (low voltage and high voltage setups), is obtained. Using the presented identification procedure, the data is processed, and the characterization is completed in the following phase. Based on experimental data, a more accurate model of aerodynamic forces and torques and electric power was obtained, compared to previous approaches. In the final phase of this research, sizing of conventional heavy-lift multirotor configurations is carried out, where the diagonal, take-off mass, hovering power, and payload capacity are considered, and results are shown graphically. The proposed sizing steps enable further performance analysis to design a more efficient system, especially from the aspect of payload capacity.

**INDEX TERMS** Electric propulsion unit, heavy-lift multirotor, multirotor configuration, payload capacity, unmanned aerial vehicles.


## I. INTRODUCTION

Unmanned aerial vehicles (UAVs) have become increasingly popular due to advancements in technology, which have encouraged the development of various types of UAVs and expanded their range of applications. UAVs can be classified in different ways, such as by endurance/range, flying height, weight/dimensions, or wing type. The most common classification is based on wing type, which includes two basic categories: fixed-wing and rotary-wing UAVs. More recently, flapping-wing and hybrid UAVs [1] have also gained attention in research. The choice of aircraft category primarily depends on the mission profile. Fixed-wing UAVs are used for missions requiring long-distance coverage, such as photogrammetric aerial mapping systems [2] or surveillance missions [3]. They require a runway or launch pad combined

with a landing system, such as Zipline drone delivery, which lands using a tail hook to catch an arresting gear [4].

On the other hand, rotary-wing UAVs have the ability to vertically take-off and land (VTOL) from relatively small and relatively flat surfaces, with the surface size depending on the UAV size. One subtype is the helicopter, which typically consists of a main rotor and a tail rotor [5]. The previously mentioned fixed-wing and helicopter UAVs are derived from their manned counterparts, which have been in use for decades. With the development of fly-by-wire technology, significant growth in the multirotor category of rotary-wing UAVs is emerging.

The multirotor type of UAV has become extremely attractive due to its relative ease of use, maneuverability, and affordability. In addition to its ability to perform VTOL and hover in place, this type of rotary-wing UAV offers a wide range of propulsion configurations that enable it to execute intricate and precise maneuvers. Furthermore, it possesses a

The associate editor coordinating the review of this manuscript and approving it for publication was Shaopeng Wu .

certain level of propulsion redundancy for added reliability. Despite their versatility, multirotors present significant challenges due to their inherent instability and highly nonlinear and multivariable nature.

Consequently, extensive efforts have been made in various research aspects in recent times. Regarding control, numerous methods are suitable, ranging from ready-to-fly solutions to new control approaches, and various multirotor configurations have been considered. For example, in a recently conducted research [6], adaptive sliding mode control based on neural networks was proposed. The researchers tested the performance and disturbance rejection through numerical simulations of a basic configuration with four rotors, a so-called quadrotor (quadcopter) UAV. Additionally, in paper [7], an efficient nonlinear adaptive weighted pseudo-inverse matrix control allocation was presented and tested on the flight performance of a six rotors conventional (planar) configuration, a so called hexarotor (hexacopter) UAV. In addition to the commonly used planar configurations with four, six, or eight (octorotor) propulsion units (rotors), numerous other designs are possible. For instance, the paper [8] introduced and validated nonlinear model predictive control for multirotor UAVs with generic configuration parameters. Advancements in various fields have made multirotors suitable for different sectors, from delivery [9], [10] to aerial robots [11], [12].

Although the advantages are numerous, it is important to emphasize that multirotor UAVs, due to their need to cancel the gravitational force with total thrust force, classify as high-energy consumption UAVs. Regarding UAV propulsion, various systems are used depending on the aircraft category. While fixed-wing aircraft are currently experiencing wider applications of various propulsion systems [13], multirotor UAVs mainly utilize electric propulsion combined with LiPo batteries. However, research is being conducted in the area of hybrid propulsion systems, including systems based on ICE driven generators [14], [15] or fuel cell systems for small aircraft propulsion [16]. The adoption of such systems still faces barriers, as outlined in [17]. Currently, multirotor UAVs with electric motor propulsion systems in combination with LiPo batteries or the aforementioned hybrid energy systems are predominately used. In research [18], electric propulsion system sizing for multirotor performance prediction and further design optimization is shown.

Due to the high-energy consumption nature, when designing a multirotor UAV, it is important to carefully select system parameters and components in order to minimize energy consumption. Numerous studies have been conducted covering various aspects ranging from energy consumption prediction [19] to sizing methodologies [20], [21]. Furthermore, in the paper [22], an analytical framework is presented for addressing hovering performance and optimal sizing of battery-powered electric multirotors. One research group focuses on estimating functional parameters and characteristics of the key components within the system [23], while further research explores efficient sizing methodologies for

electric multirotor vehicles enabling configuration optimization for different missions and requirements [24]. Since increasing propulsion forces and torques can be achieved with a larger number of rotors, conventional configurations discussed in previous works tend to result in larger-sized multirotor UAVs. However, compact coaxial configurations have been investigated, with various papers demonstrating their efficiency and achieving improvements [25]. Propulsion units of sizes up to 100 N were tested [25], and mentioned in the context of heavy-lift (large payload) multirotor UAVs, as also presented in the paper dealing with the design methodology of UAVs with coaxial rotors [26].

In research aimed at testing the performance of large-scale tandem UAVs [27], electric propulsion units (EPU) consisting of a 28\*8.4" propeller and U8 100 Kv motor were experimentally tested. An improved model of the electric propulsion system was presented in [28], where three EPU setups were experimentally tested. This research focuses on the armature reaction of the motor, effectively explaining the significant performance degradation during high-power operation. Additionally, paper [29] presents a method for dimensioning an electric propulsion system for designing and manufacturing a multirotor UAV. An agricultural quadrotor with a payload of 10 kg was built and compared with the sizing results. In cited research, small-scale sets were tested experimentally, or sets were tested within a certain range, and further analysis was carried out using mathematical models. A review of the literature did not find a paper on the subject of experimental characterization of the heavy-lift propulsion system that covers a very wide range in terms of forces and powers of the propulsion units, therefore, in this research, a wide range up to 250 N and 6 kW is investigated.

## A. CONTRIBUTIONS

In this study, the experimental characterization of EPU designed for powering heavy-lift multirotor UAVs is carried out. Therefore, extensive testing of two EPU series (low voltage and high voltage) in a wide range of power and size was carried out for a total of 28 EPU setups. To enable the process of EPU characterization, a framework consisting of data acquisition and data processing is presented. The first contribution of this paper is a more accurate model of the heavy-lift electric multirotor propulsion system, compared to simplified models that are commonly used or compared to a variety of introduced approaches that rely on mathematical models for the estimation of parameters. The characteristics of thrust force, drag torque, and electric power, based on experimental data, are presented. The second contribution in the paper is a systematic representation of the heavy-lift multirotor UAV sizing relations, regarding diagonal, take-off mass, hovering power, and payload capacity. The proposed approach emphasizes payload capacity as a key aspect, given that the research discussed heavy-lift configurations, and such an approach, based on experimental data, is not covered in the literature. The major goal of the presented sizing approach is to enable a more efficient selection of the main

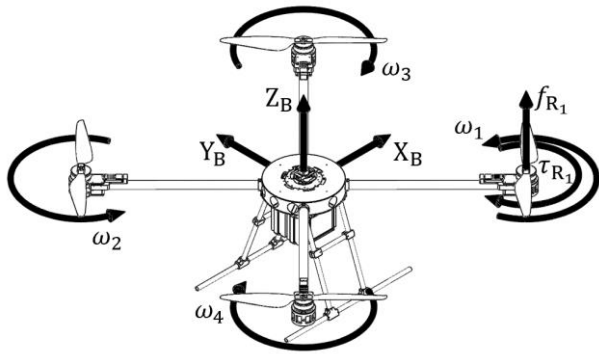


**FIGURE 1.** Multirotor UAV reference coordinate system and rotor angular velocities.

system parameters, and the results are graphically presented for a total of 84 configurations.

**B. ORGANIZATION**

In section II electric multirotor UAV system is briefly described. Section III is divided into a description of experimental hardware, an explanation of data acquisition and processing, and finally characterization of EPU setups with efficiency comparison. Section IV presents the sizing of heavy-lift multirotor UAVs. Finally, conclusions are given in section V.

**II. PRELIMINARY ELECTRIC MULTIROTOR UAV SYSTEM DESCRIPTION**

When describing multirotor UAVs, it is important to emphasize that regardless of the configuration, these aircraft are highly non-linear, inherently unstable, multivariable, and have high energy consumption. From a system modeling and mechanical perspective, a multirotor can be defined as a rigid body with the only moving parts being the rotors of the propulsion system. The equations of motion can be derived using the Newton-Euler method [30] and are represented by six second-order differential equations. The first three degrees correspond to translational dynamics, while the last three correspond to rotational dynamics. The dynamics of the multirotor are defined with respect to the body frame (\$\mathcal{F}^B\$) established by \$\{O\_B, X\_B, Y\_B, Z\_B\}\$, as shown in Fig. 1, and is given by the expression,

$$\dot{v} = M_B^{-1} (-C_B(v)v + g_B + d + u_B). \tag{1}$$

To obtain the acceleration vector defined with respect to the body frame \$\dot{v} = [\dot{u} \ \dot{v} \ \dot{w} \ \dot{p} \ \dot{q} \ \dot{r}]^T\$, the matrix \$M\_B\$ needs to be defined which contains mass and moments of inertia. Assuming that the \$O\_B\$ is located at the multirotor’s center of gravity (CoG) and the main axes of inertia coincide with the body frame axis \$\{X\_B, Y\_B, Z\_B\}\$, since the multirotor airframe is symmetrical for considered configurations, the body’s inertia tensor becomes a diagonal matrix, resulting in a diagonal matrix \$M\_B = \text{diag} \{m, m, m, I\_{xx}, I\_{yy}, I\_{zz}\}\$. Moreover,

\$C\_B(v)\$ represents Coriolis and the centripetal matrix [31] that account for the rotation of the body frame. In a stationary state (hovering), the gravitational force \$g\_B\$ acts along the \$Z\_B\$ axis and should be cancelled out and is generally related to translational dynamics. Therefore the UAV mass (\$m\$) plays a crucial role in system design which includes system components, airframe parts, and payload. For heavy-lift multirotor UAVs used in payload dispersal such as in agriculture sector, the payload mass can be time-dependent, denoted as \$m(t)\$. Unmodeled dynamics (gyroscopic effect, air resistance, etc.) and external disturbances such as wind gusts are represented by the vector \$d\$.

In terms of control and flight planning, the control vector \$u\_B = [f\_X \ f\_Y \ f\_Z \ \tau\_\phi \ \tau\_\theta \ \tau\_\psi]^T\$, with respect to the body frame, represents the mapped thrust forces \$f\_R = [f\_{R1} \ f\_{R2} \ \dots \ f\_{RN}]^T\$ and drag torques \$\tau\_R = [\tau\_{R1} \ \tau\_{R2} \ \dots \ \tau\_{RN}]^T\$ generated by the rotation of the propellers at each rotor. The control vector can be defined by the following expression,

$$u_B = \begin{bmatrix} H \\ \Xi \end{bmatrix} f_R + \begin{bmatrix} 0_{3 \times N} \\ H \end{bmatrix} \tau_R. \tag{2}$$

The matrices used for mapping are determined by the geometric arrangement of the propulsion configuration. The first matrix \$H (\mathbb{R}^{3 \times N})\$ describes the rotor orientations and the second matrix \$\Xi (\mathbb{R}^{3 \times N})\$ is composed of vector products of rotor position and orientation, which map the thrust force to control moments. The matrix \$\Xi\$ is derived using the matrix representation of the vector product \$a \times b = S(a)b\$, as shown in previous research [32]. It is important to emphasize that conventional multirotor configurations have a planar arrangement of the rotors, making the rotor orientation vectors unit vectors. As a result, regardless of the number of rotors, conventional configurations are underactuated systems. Moreover, since changing the position requires changing the orientation, they are also defined as coupled dynamics systems.

**A. MULTIROTOR ELECTRIC PROPULSION SYSTEMS**

Electric Multirotor UAVs consist of \$N\$ rotors, which represent EPUs, as shown in Fig. 2 for the quadrotor configuration. In general, EPU setups consist of a fixed-pitch propeller mounted on a brushless DC (BLDC) motor rotor, which is driven by the electronic speed controller (ESC). Regarding the fixed-pitch propeller, thrust force, and drag torque will be investigated, while the other aerodynamic effects are neglected. The required thrust forces, and consequently drag torques, are achieved by changing the angular velocity, i.e., the RPM of the rotor. The propeller geometry, where the main parameters are diameter, pitch angle, and number of blades, influences the amount of induced airflow. Larger parameters of propeller geometry, where further diameter will be investigated, in addition to increasing the thrust force, generate higher drag torque. Therefore, a combination with higher torque BLDC motors is required. A simplified model is often used in which the thrust force is proportional to the

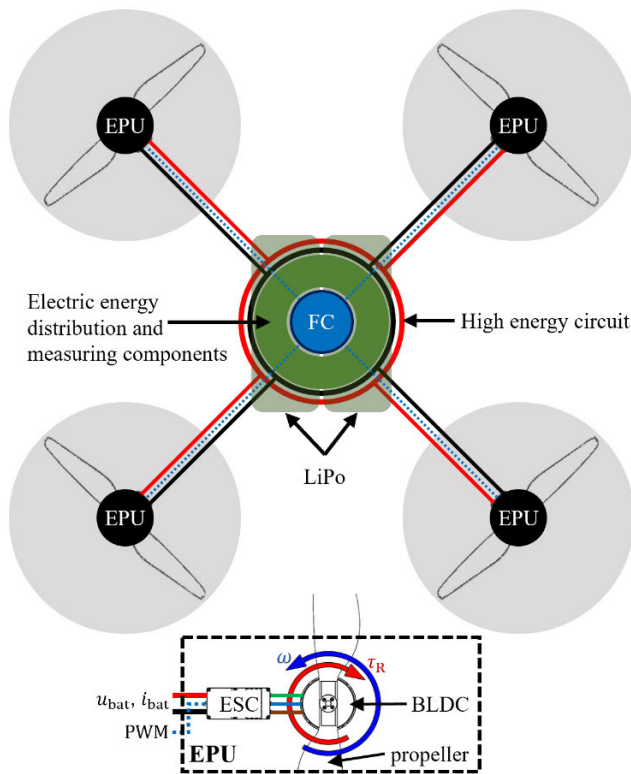


FIGURE 2. Electric multirotor UAV topology.

square of the angular velocity of the rotor,  $f_{R_i} = k_{f_i} \omega_i^2$ , where  $k_{f_i}$  is the thrust force factor. The drag torque to be overcome by the BLDC motor can also be modeled as  $\tau_{R_i} = k_{\tau_i} \omega_i^2$ , where  $k_{\tau_i}$  is the drag torque factor.

The BLDC motor is an electric motor driven by an ESC that utilizes electronic commutation to provide high efficiency, reliability, and precise control. Electromagnets (armature) are located on the stator, while the rotor consists of permanent magnets which are in the case of outrunner motors positioned outside the stator. There is a large range of BLDC motors, from micro ones used to propel micro aerial vehicles (MAVs), with the power of several tens of watts, to motors used for the heavy payload with a power of several kilowatts. The main BLDC parameters that will be further considered are the motor size, mass, and velocity constant  $K_v$ , which defines the number of revolutions per applied voltage in the case without load. The ESC used to drive the BLDC motor is an integrated power inverter that converts supplied DC voltage into appropriate phase voltages. The ESC consists of a microcontroller that processes the input PWM signal and switches transistors. The input PWM defines the switching rate of transistors and consequently the voltage fed to phases. With a higher duty cycle of the PWM, the motor angular velocity is increased. The main parameters for selecting the ESC are the operating voltages expressed in the number of battery cells and the maximum allowed current, which has to be 20% higher than the maximum motor current to avoid overheating or failure.

TABLE 1. Low-voltage EPU setups and related components.

LV Setup	BLDC Designation	Kv	ESC (6S)	propeller
S01	MN4014	400	Air 40A	P17*5.8"
S02	MN5212	340	Air 40A	P17*5.8"
S03	MN5212	340	Air 40A	P18*6.1"
S04	MN501-S	360	Flame 40A	P18*6.1"
S05	U7	280	Flame 70A	P20*6"
S06	U7	280	Flame 70A	P22*6.6"
S07	MN6007	320	Flame 70A	P20*6"
S08	MN6007	320	Flame 70A	P22*6.6"
S09	P60	340	Alpha 60A	P20*6"
S10	P60	340	Alpha 60A	P22*6.6"
S11	P60	340	Flame 70A	P20*6"
S12	P60	340	Flame 70A	P22*6.6"
S13	MN701-S	280	Flame 100A	P24*7.2"
S14	MN701-S	280	Flame 100A	G26*8.5"

TABLE 2. High-voltage EPU setups and related components.

HV Setup	BLDC Designation	Kv	ESC (12S)	propeller
S01	MN1005	90	Flame 60A	G30*10.5"
S02	MN1005	90	Flame 60A	G32*11"
S03	U11	120	Flame 100A	G26*8.5"
S04	U11	120	Flame 100A	G28*9.2"
S05	P80	100	Alpha 80A	G30*10.5"
S06	P80	100	Alpha 80A	G32*11"
S07	P80	100	Flame 100A	G30*10.5"
S08	P80	100	Flame 100A	G32*11"
S09	U12	120	Flame 180A	G28*9.2"
S10	U12	120	Flame 180A	G30*10.5"
S11	U13	130	Alpha 120A	G30*10.5"
S12	U13	130	Alpha 120A	G32*11"
S13	U13	130	Flame 180A	G30*10.5"
S14	U13	130	Flame 180A	G32*11"

With electric multirotors, LiPo batteries are used as a conventional energy source, providing high energy density and discharge rate to enable a consistent energy flow to the propulsion system (module). Multirotor UAVs consist of one or more batteries (battery packs) determined by the number of cells, capacity, and mass. This paper focuses on investigating the low voltage (LV) energy module setup, which utilizes 6-cell (6S) batteries, and a high voltage (HV) setup with 12-cell (12S) batteries. In addition to batteries, there are also distribution and measuring elements that represent the interface between the energy and propulsion, the propulsion and control, and the control and energy module.

## B. DESIGN CONSIDERATIONS FOR HEAVY PAYLOAD ELECTRIC PROPULSION

As part of this research, a total of 28 EPU setups were considered, covering a wide range of heavy lift multirotor propulsion, whether viewed from the aspect of aerodynamic forces, power, or size. Table 1 shows 14 LV setups, and Table 2 shows 14 HV setups for which identification and



characterization is carried out. Experimental data is obtained based on which the identification is conducted.

### III. ELECTRIC PROPULSION UNIT IDENTIFICATION AND CHARACTERIZATION

In this section, the characterization of the considered EPU setups is presented based on conducted experimental measurements utilizing measuring equipment and investigated EPU components. Procedures for data acquisition using RCbenchmark software and data processing using the MATLAB software package are used to generate EPU characteristics.

#### A. EXPERIMENTAL SETUP HARDWARE

To effectively carry out the identification of EPU parameters, it is crucial to select measuring equipment and software. The selected equipment should cover the measuring range for the considered EPU setups, and the software is partly open-source. Choosing the Series 1780 test stand [33] from Tyto Robotics, with associated RCbenchmark software ensures accurate and reliable data acquisition during the experimental process. The test stand which is shown in Fig. 3 consists of a construction assembly whose main elements are the ground railing system and two sets of plate support, which enables the measurement of coaxial setups as well. To measure aerodynamic forces ( $f_R$ ) and torques ( $\tau_R$ ), load measurement units (A and B side) comprising three load cell sensors are utilized. The selected 1780 test stand enables the measurement ranges up to 400 N and 18 Nm. Load cell sensors are connected to the sensor chain, which is further connected to the dual main board. The rotor RPM is measured through an optical probe that counts RPMs by detecting a reflective motor marker. The optical probe is mounted to the motor mount plate and connected to the sensor chain. Additionally, a tachometer DT-2259 is used to check the RPM measured by the optical probe, where for each setup, validation is considered in the entire RPM range without load (propeller).

The motors are mounted on the load measurement unit via an assembly plate and are connected to the ESC using a no-solder board mounted on a two-plate support that enables quick replacement of motors or ESCs. The ESC, on the other side, is connected to the power and control console in which power sensors and control board are integrated and connected to the dual main board. The power and control console measures the voltage and current (up to 150 A) between ESC and the connected LiPo battery and is responsible for the control signal sent to ESC. Measurements are performed using Gens ace Tattu batteries with a capacity of 16 Ah, for both LV and HV series. In addition to the mentioned mechanical and electrical quantities, the motor and ESC temperature can be monitored by using additional temperature sensors. Instead of temperature probes that have slow dynamics, a thermal imaging camera is utilized to monitor the temperature of the components.

From the aspect of data acquisition, the main board is connected with a USB cable to a computer with the RCbench-

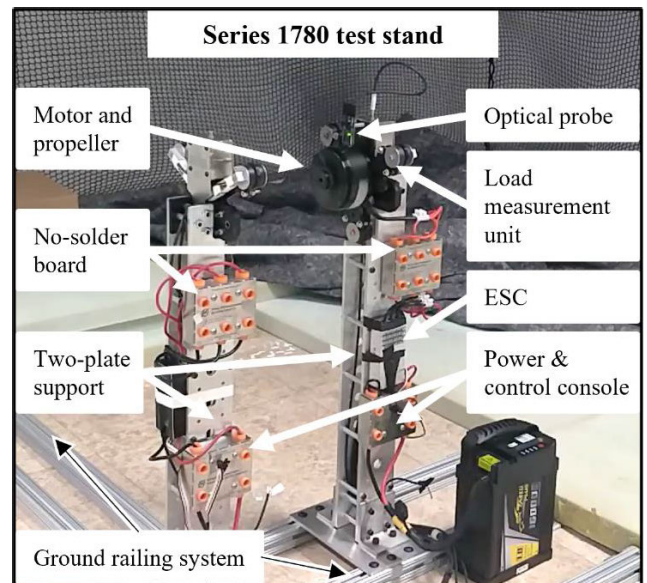


FIGURE 3. Tyto Robotics series 1780 experimental test stand.

mark software installed. Measurement parameters and safety settings are adjusted in the software, which also includes debugging tools. There are two basic modes of operation, manual control where individual PWM signals are sent to hardware, and automatic control. Since the goal is to have unified measurements, automatic control mode is used deploying a modified RCbenchmark software measurement script. After each measurement cycle is done, the.csv file is automatically generated.

#### B. DESCRIPTION OF THE PROPULSION CHARACTERIZATION FRAMEWORK

Given that this work investigates the experimental identification of propulsion units intended for heavy-lift multirotor UAVs, additional attention should be paid to safety aspects. First, the experimental hardware is placed inside a cage that is surrounded by a net, while the computer for data acquisition is located behind a panel fence. Furthermore, every time the setup is changed (whether it is a change of motor, propeller, or ESC), the same is done when the power source (LiPo battery) is disconnected. Before each measurement, initially, the RPM is checked in a case without load, considering that the RPM probe needs to be adjusted since the motors are of different dimensions, primarily diameter. The measurement of the RPM is sensitive to the lighting, the distance between the probe and the motor, motor marking, and other effects therefore, it is necessary to check the probe in manual operation mode before the automated measurement. After the RPM measurement is validated using a tachometer, the propeller is mounted and in manual mode, a second check is conducted. Quick measurement of the thrust force and drag torque is performed and briefly analyzed. At the same time, the sign of the thrust force and the drag torque, which can be adjusted by software, is checked. Once the checks have been made, the automated measurement proceeds.

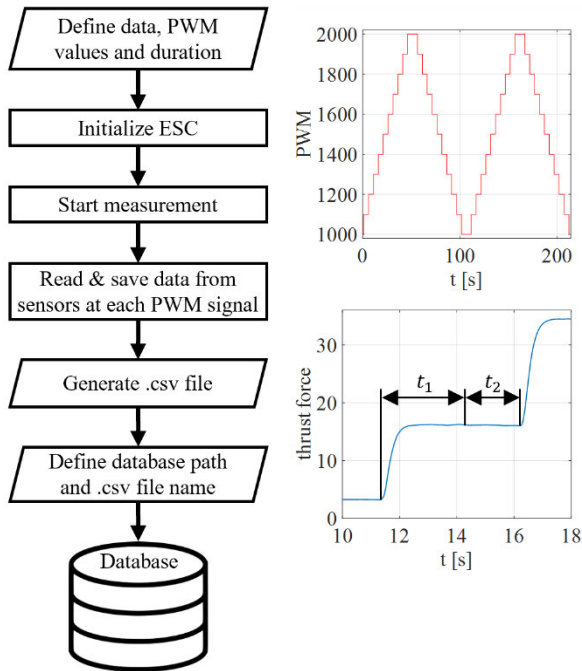


FIGURE 4. Data acquisition flowchart for an automated measurement cycle.

Fig. 4 shows the data acquisition flow chart together with a graphic representation of the reference state and a cut of one measurement cycle values for one of the measured parameters. The modified script for automated measurement is executed through the RCbenchmark software, where the reference state is defined by the duration and values of the PWM signals. After the ESC is initialized, the measurement cycle begins. For each reference value of the PWM, the values from the sensors are read and saved. Every PWM signal is held constant for 8 s after which the PWM increases or decreases by 100 depending on the step of the measurement cycle. Time at each PWM is divided into settling time ( $t_1$ ) which lasts 3 seconds and sampling time ( $t_2$ ) which lasts 2 seconds. Based on 80 samples, the script gives the mean value of the measured values for a certain PWM signal. Upon completion of the measurement cycle, the.csv file is automatically generated in which the rows represent the actual PWM signal sent to ESC and columns represent the measured values (i.e., thrust force, drag torque, RPM, voltage, current, power, and others). In the last step, the database path and.csv file name are defined, which ends the data acquisition process.

In the second step, the identification of EPU is carried out based on experimental measurements which are stored in the database. The generated.csv files were loaded, processed, and graphically presented using the MATLAB software package. The flow chart of the identification procedure is shown in Fig. 5, alongside a graphic representation of the raw measurement of one cycle, and a static map for the thrust force of one EPU setup. For the selected folder, the script searches for.csv files in all subfolders and saves their paths. In the next step,

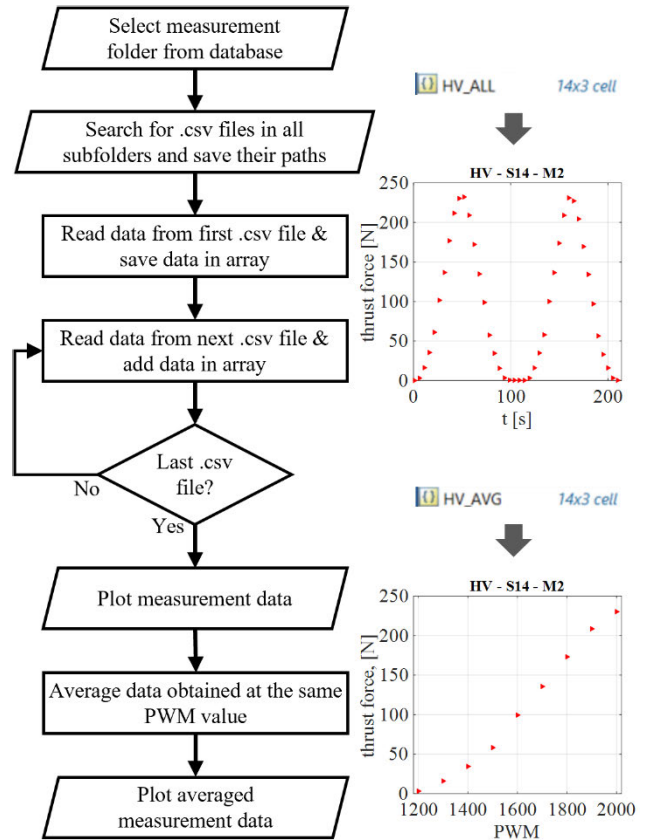


FIGURE 5. EPU identification procedure flowchart.

it reads the data from the first.csv file and saves the data in an array, then it reads the next.csv file until it reaches the last file. Both, in the case of LV or HV setup measurements, the data is saved in an array which is in MATLAB represented as a  $14 \times 3$  cell. Each cell represents one measurement cycle (14 setups and three voltage levels). Each measurement cycle can be viewed as a matrix, where rows represent PWM signals, and columns represent, along with time and the reference PWM signal, the measured values (thrust force, drag torque, and others). Once the array is filled with data from all measurements, measurement data can be plotted as shown for thrust force related to cycle time for HV S14 setup and second measurement. In the next step, obtained measurement data is averaged at the same PWM values. Output vectors that will be used for further characterization can be plotted as static maps regarding the PWM signal.

The process of parameter identification enables the representation of static maps of the EPU setups based on experimental data for mechanical and electrical quantities. From the aspect of control implementation, the static maps related to thrust force and drag torque can be further linearized and implemented in the control system. From the aspect of multirotor hardware design, the experimental data stored in the array will be used to perform the characterization of EPU. In this work, the following parameters were considered for characterization purposes: thrust force, drag torque, electric power, and overall efficiency.

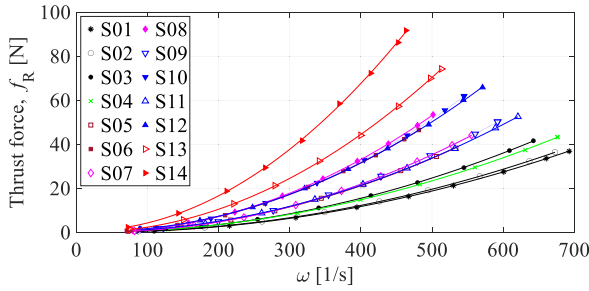


FIGURE 6. Thrust force characteristics as a function of rotor angular velocity for LV EPU setups.

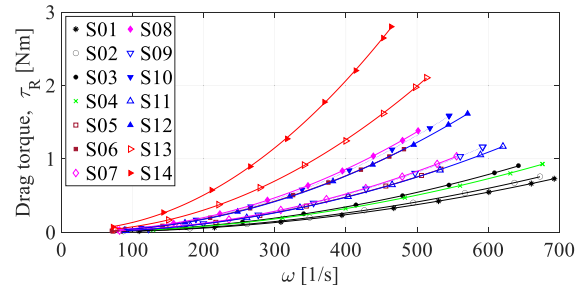


FIGURE 8. Drag torque characteristics as a function of rotor angular velocity for LV EPU setups.

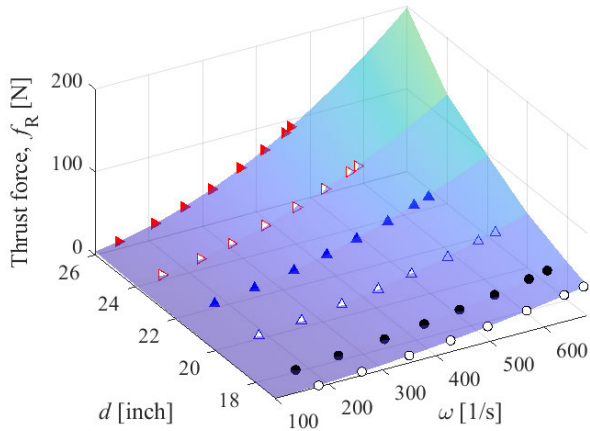


FIGURE 7. Thrust force as a function of rotor angular velocity with respect to propeller diameter for LV EPU setups.

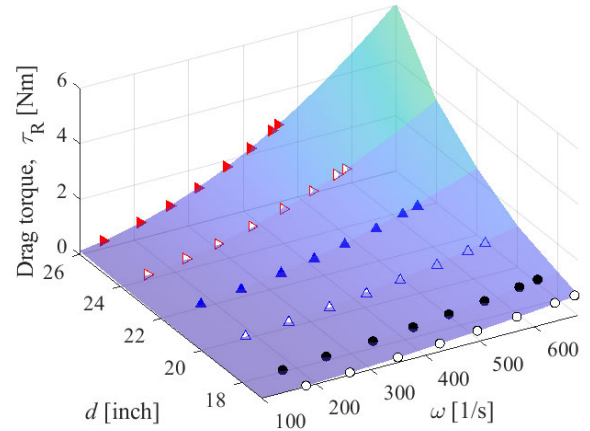


FIGURE 9. Drag torque as a function of rotor angular velocity with respect to propeller diameter for LV EPU setups.

TABLE 3. Polyfit thrust force function coefficients for LV EPU setups.

$d$	$f_2$	$f_1$	$f_0$
17''	0.8395e-04	-0.0037055	0.01270526
18''	1.0190e-04	-0.0028798	-0.0381144
20''	1.5252e-04	-0.0076071	0.26272317
22''	2.2528e-04	-0.0109789	0.37854719
24''	2.9609e-04	-0.0077324	0.16783609
26''	4.3925e-04	-0.0084515	0.70673919

TABLE 4. Polyfit drag torque function coefficients for LV EPU setups.

$d$	$\tau_2$	$\tau_1$	$\tau_0$
17''	1.6408e-06	-0.0000340	0.00206408
18''	2.1469e-06	-0.0000303	0.00319094
20''	3.4194e-06	-0.0001344	0.00915262
22''	5.6348e-06	-0.0002900	0.01978160
24''	8.3626e-06	-0.0002261	0.01333771
26''	13.550e-06	-0.0003340	0.03185438

C. ELECTRIC PROPULSION UNIT LOW-VOLTAGE SERIES CHARACTERISTICS

In the first part of the EPU characterization, thrust forces were analyzed in dependence on the angular velocity of the rotor. In Fig. 6, markers show experimentally obtained values for 14 LV setups that were shown in Table 1. Then, based on the experimental data, polynomial curve fitting is conducted using MATLAB polyfit function. Thrust force second-order characteristics were given with the following expression,

$$f_R = f_2\omega^2 + f_1\omega + f_0. \tag{3}$$

The characteristics are represented by lines in Fig. 6 where it is evident that the coefficients primarily depend on the geometry of the propeller, where the propeller diameter ( $d$ ) will be further investigated. Given that 14 LV setups cover the 17-26'' propeller range, and the research employed propellers with six distinct geometry settings, MATLAB mean function is used in order to obtain the coefficients of the characteristics related to propeller diameter which are shown in Table 3.

Fig. 7 shows the characteristics according to Table 3, and the same graph shows the experimental values for individual EPU setups (S02, S03, S11, S12, S13, S14). From the point of view of UAV design, the considered mathematical formulation based on experimental data can more accurately describe the thrust force related to the angular velocity of the rotor, compared to the commonly used models.

During the second part of the EPU characterization, the drag torque is shown also related to the angular velocity of the rotor. The same steps as in the thrust force analysis were carried out, and the drag torque characteristic is given by the following expression,

$$\tau_R = \tau_2\omega^2 + \tau_1\omega + \tau_0. \tag{4}$$

As well as thrust force, drag torque experimental data is shown using markers, and the characteristics are represented by lines in Fig. 8. Drag torque characteristics are shown in Fig. 9, according to coefficients in Table 4 alongside experimental data (S02, S03, S11, S12, S13, S14).



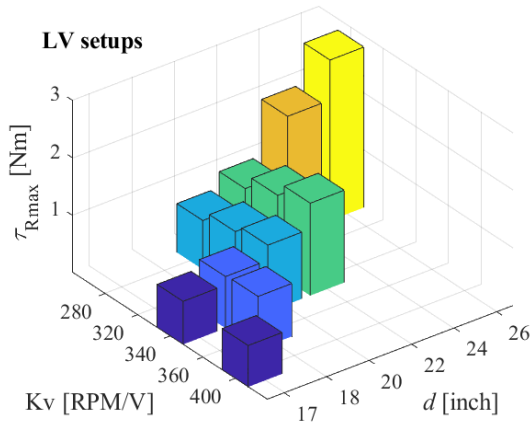


FIGURE 10. Maximum drag torque concerning propeller diameter and motor velocity constant for LV EPU setups.

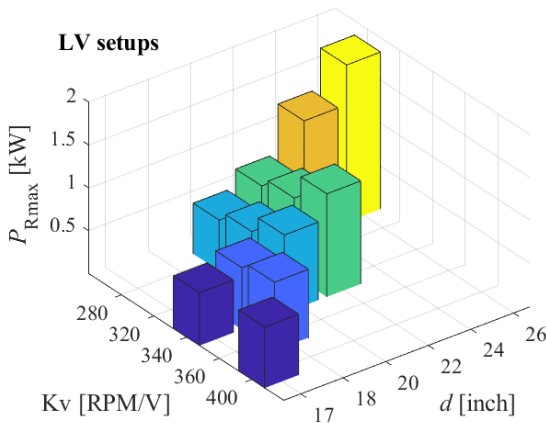


FIGURE 11. Maximum electric power concerning propeller diameter and motor velocity constant for LV EPU setups.

Comparable to the often-used mathematical formulation where the thrust force and drag torque are proportional to the square of the angular velocity, the considered formulation provides a more precise model, resulting in more realistic simulations and more efficient parameter selection in the system design phase. The formulation can be further simplified considering that the  $f_0$  and  $\tau_0$  can be neglected.

When sizing an EPU for a multirotor type of UAV, apart from the consideration of propeller diameter, the BLDC motor velocity constant is the next key factor to examine carefully.

BLDC motor velocity constant  $K_v$ , is expressed in RPM per volt (without load), therefore determines the angular velocity of the rotor. To drive a propeller of a certain diameter, motors with a higher  $K_v$  must have a higher torque to be able to produce higher thrust forces. The higher torque also leads to an increase in power (energy) consumption.

Fig. 10 shows the maximum drag torques for LV setups (S01, S02, S03, S04, S05, S06, S07, S08, S11, S12, S13, S14) depending on the diameter and  $K_v$ . Fig. 11 shows the

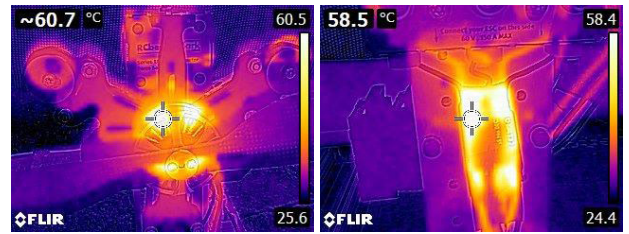


FIGURE 12. LV BLDC motor and ESC heating obtained by thermal imaging camera.

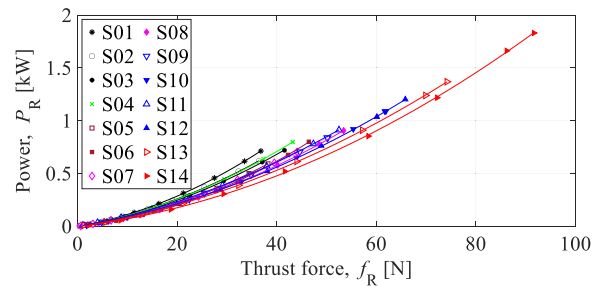


FIGURE 13. Electric power characteristics as a function of thrust force for LV setups.

maximum powers for the same LV setups regarding diameter and  $K_v$ . It should be emphasized here that the maximum torque and maximum power depend on the state of charge of the battery. The graphs show the values for the second measurement (M2). When designing a propulsion system, one of the key steps is selecting the appropriate motor and propeller combination in order to achieve higher efficiency. The goal is to find the right balance between speed and torque and to ensure that the motor is not overloaded, which can cause it to overheat and potentially stop running. During the experiments, the BLDC and ESC temperatures were periodically recorded as shown in Fig. 12 and were within the range specified in the components datasheet.

Given that the multirotor dynamics is dominantly influenced by the propulsion configuration thrust forces, the relationship between the thrust force and power is crucial in designing the propulsion configuration. Power functions regarding thrust force, shown in Fig. 13 can be described with second-order characteristics

$$P_R = P_2 f_R^2 + P_1 f_R + P_0, \quad (5)$$

where the coefficients for 14 LV setups are given in Table 5. As expected, setups with a larger propeller diameter consume less power per thrust force, however, it should be taken into account that with a more powerful EPU, the mass of the propulsion unit is consequently increased. This information will be discussed when sizing the overall system.

#### D. ELECTRIC PROPULSION UNIT HIGH-VOLTAGE SERIES CHARACTERISTICS

As shown in the EPU LV series characterization procedure, the same steps will be performed for the HV series whose



TABLE 5. Polyfit electric power function coefficients for LV EPU setups.

LV Setup	$P_2$	$P_1$	$P_0$
S01	3.0147e-04	0.00833920	-0.0021359
S02	2.4400e-04	0.00818561	-0.0023873
S03	2.3059e-04	0.00785364	-0.0021560
S04	2.4078e-04	0.00812245	-0.0024719
S05	2.4698e-04	0.00605201	-0.0015998
S06	2.7200e-04	0.00451477	0.00048126
S07	1.9628e-04	0.00746628	-0.0028541
S08	1.9389e-04	0.00666757	-0.0033482
S09	1.7606e-04	0.00794843	-0.0034784
S10	1.6326e-04	0.00760261	-0.0040801
S11	1.7424e-04	0.00828599	-0.0022628
S12	1.6325e-04	0.00755050	-0.0033894
S13	1.5016e-04	0.00736001	-0.0052216
S14	1.5540e-04	0.00578834	-0.0027486

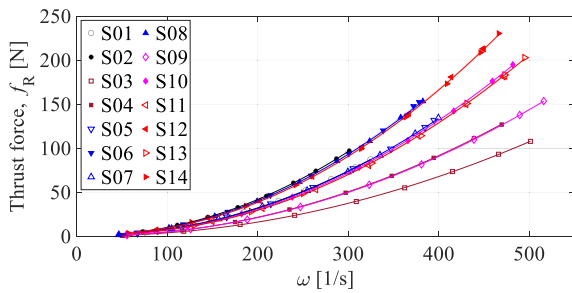


FIGURE 14. Thrust force characteristics as a function of rotor angular velocity for HV EPU setups.

setups are shown in Table 2. Thrust force experimental results and the characteristics of each setup are shown in Fig. 14. As in the case of the LV series, the thrust force is shown as second-order characteristics regarding rotor angular velocity. Given that 14 HV setups cover the 26-32" propeller range, and the research was conducted using four different propellers, coefficients of thrust force are given in Table 6. The characteristics according to Table 6 and experimental values for individual EPU setups (S03, S04, S09, S10, S13, S14) are shown in Fig. 15, to compare the mathematical formulation with experimental data.

Although the motor constants of the HV setups are more than twice as low as the LV setups, they run at twice the voltage (12S LiPo). Next, drag torque is shown in Fig. 16 for experimental data and second-order characteristics regarding the angular velocity of the rotor. Drag torque characteristics coefficients are given in Table 7. Like the thrust force, the characteristics of drag torque are presented in Fig. 17, following Table 7, alongside the experimental data. From the aspect of the analysis of aerodynamic forces and torques, the range of the HV series continues to the LV EPU series.

As with the LV setup, further in Fig. 18 is shown the maximum drag torques for HV setups (S01, S02, S03, S04, S05, S06, S07, S08, S11, S12, S13, S14) depending on the

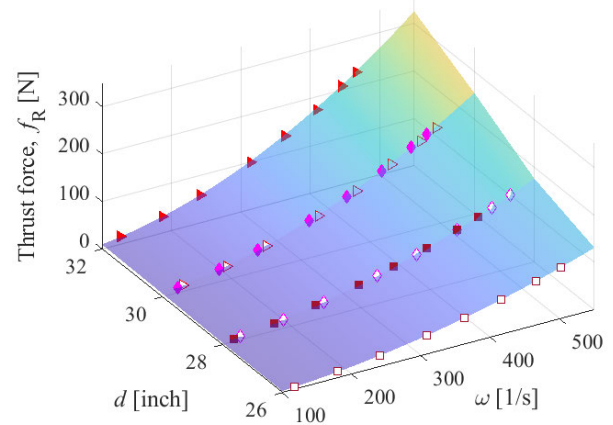


FIGURE 15. Thrust force as a function of rotor angular velocity with respect to propeller diameter for HV EPU setups.

TABLE 6. Polyfit thrust force function coefficients for HV EPU setups.

$d$	$f_2$	$f_1$	$f_0$
26"	4.5394e-04	-0.0137426	0.66601179
28"	6.1045e-04	-0.0177129	0.51850525
30"	9.0343e-04	-0.0373933	2.18964923
32"	11.491e-04	-0.0437827	2.34873961

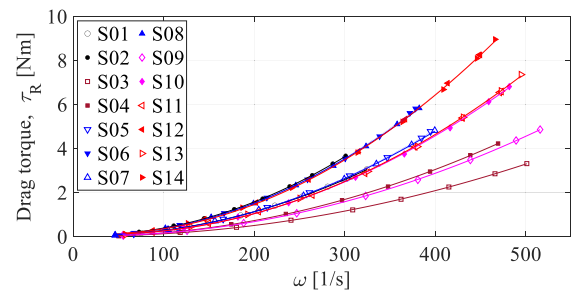


FIGURE 16. Drag torque characteristics as a function of rotor angular velocity for HV EPU setups.

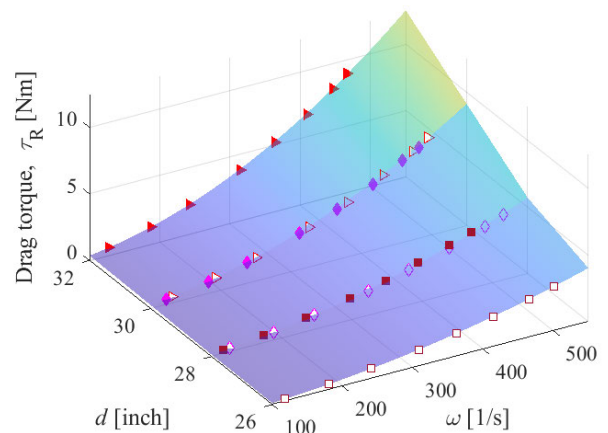


FIGURE 17. Drag torque as a function of rotor angular velocity with respect to propeller diameter for HV EPU setups.

propeller diameter and motor constant Kv. Fig. 19 shows the maximum powers for the same HV setups where both graphs are obtained from the second measurement (M2). From the

TABLE 7. Polyfit drag torque function coefficients for HV EPU setups.

$d$	$\tau_2$	$\tau_1$	$\tau_0$
26"	1.3841e-05	-0.0003930	0.03428070
28"	1.9707e-05	-0.0005338	0.02647627
30"	3.2853e-05	-0.0016823	0.11606717
32"	4.5060e-05	-0.0022318	0.14555008

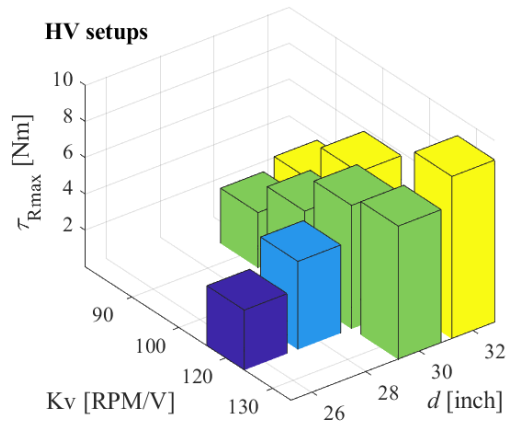


FIGURE 18. Maximum drag torque concerning propeller diameter and motor velocity constant for HV EPU setups.

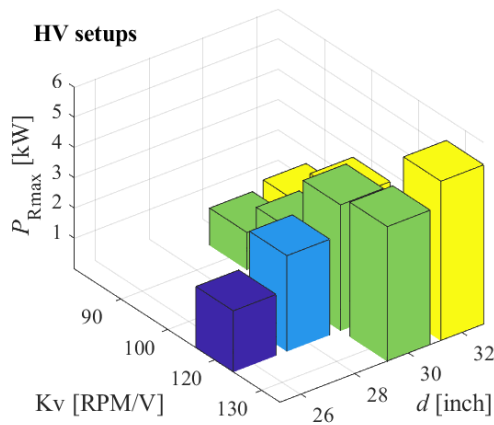


FIGURE 19. Maximum electric power concerning propeller diameter and motor velocity constant for HV EPU setups.

results shown, it is evident that there is an overlap of the range of LV and HV setups regarding drag torque and power and consequently thrust force.

During the experiments, the BLDC and ESC temperatures were systematically recorded for S11, S12, S13, and S14. Fig. 20 shows the temperature of the BLDC motor and the ESC that make up S14, immediately after the second measurement. Regardless of whether components belong to the LV or HV setups, both the Alpha and Flame series of ESC feature a passive heatsink. It is important to take the temperatures of the propulsion components into account from

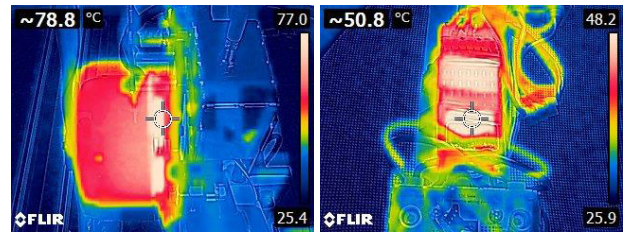


FIGURE 20. EPU S14 BLDC motor and ESC heating obtained by thermal imaging camera.

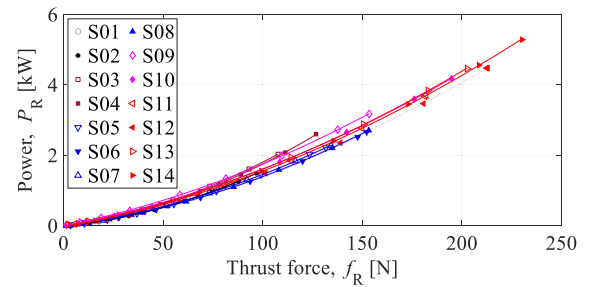


FIGURE 21. Electric power characteristics as a function of thrust force for HV setups.

TABLE 8. Polyfit electric power function coefficients for HV EPU setups.

LV Setup	$P_2$	$P_1$	$P_0$
S01	3.0147e-04	0.00833920	-0.0021359
S02	2.4400e-04	0.00818561	-0.0023873
S03	2.3059e-04	0.00785364	-0.0021560
S04	2.4078e-04	0.00812245	-0.0024719
S05	2.4698e-04	0.00605201	-0.0015998
S06	2.7200e-04	0.00451477	0.00048126
S07	1.9628e-04	0.00746628	-0.0028541
S08	1.9389e-04	0.00666757	-0.0033482
S09	1.7606e-04	0.00794843	-0.0034784
S10	1.6326e-04	0.00760261	-0.0040801
S11	1.7424e-04	0.00828599	-0.0022628
S12	1.6325e-04	0.00755050	-0.0033894
S13	1.5016e-04	0.00736001	-0.0052216
S14	1.5540e-04	0.00578834	-0.0027486

the aspect of designing propulsion airframe parts that are mechanically and thermally loaded.

As well as for LV series, power characteristics regarding thrust force, are shown for HV series in Fig. 21, alongside experimental data, and coefficients are given in Table 8. In this research, the EPU components were carefully selected to facilitate the transition from LV to HV setups across various sizing aspects. A wider range of systematically selected EPUs allows for a more comprehensive analysis of heavy-lift multirotor UAVs.

Regarding characterization, the first contribution of this research is a more accurate propulsion model based on experimental data for a wide power range of LV and HV

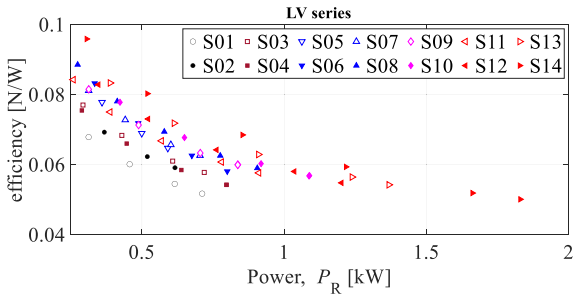


FIGURE 22. The overall efficiency with respect to electric power for LV series.

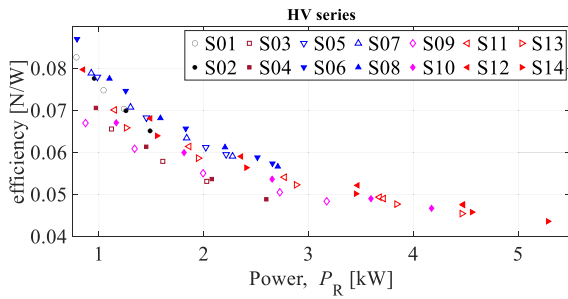


FIGURE 23. The overall efficiency with respect to electric power for HV series.

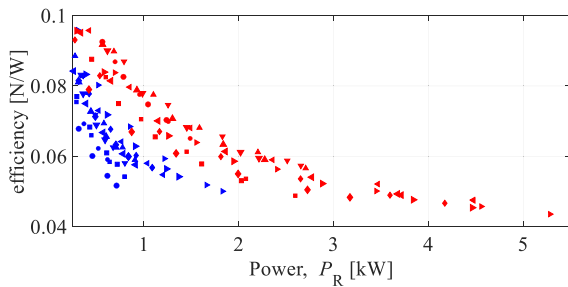


FIGURE 24. Comparison of the overall efficiency of LV and HV series.

EPU. The presented characteristics allow for the prediction of performance in electric multirotor propulsion system. This systematic approach enhances the ability to address the requirements associated with heavy-lift multirotor UAVs.

**E. COMPARISON OF THE EFFICIENCY OF LOW VOLTAGE AND HIGH VOLTAGE SETUPS**

To achieve optimal performance for a multirotor, it is inevitable to analyze the efficiency of the propulsion units. Therefore, the overall efficiency of the EPU was represented by the ratio of thrust force and electric power and is shown as a function of electric power (energy consumption). Fig. 22 shows the overall efficiency of the LV series, while Fig. 23 shows the efficiency of the HV series.

The combination of the BLDC motor and propeller is important to obtain optimal performance. The tested HV series, which encompass a range of larger propeller diameters compared to the tested LV series, generally have a higher efficiency. This observation is depicted in Fig. 24,

where the LV setups are represented by blue and the HV setups by red markers. With regard to the design of the multirotor system, it is also important to take into account the masses of the propulsion components and the energy components (LiPo batteries), which differ depending on the setup.

**IV. HEAVY-LIFT MULTIROTOR UAV SIZING**

In this section, the sizing of heavy-lift multirotor UAVs is presented, and the key parameters and characteristics of the UAV design and their impact on multirotor performance are analyzed. In this research discussed are: the size of the UAV expressed through the diameter ( $D$ ), the configurations take-off mass ( $m_{ToM}$ ), the hovering power ( $P_{hover}$ ), and finally the sizing according to the payload capacity ( $m_{PL}$ ) which is essential regarding heavy payload missions. Sizing will be shown for three conventional configurations with a generic airframe shown in Fig. 25 and regarding two experimentally characterized series of EPU setups.

**A. MULTIROTOR UAV GEOMETRIC SIZE**

The size of a multirotor UAV is influenced by the basic parameters of the propulsion configuration, the number of rotors ( $N$ ), and the diameter of the propeller ( $d$ ), which results in the expected diameter of the multirotor propulsion system. Regarding multirotor UAV design, the diameter (diagonal) defines the length of the rotor arm, whereas, from the modeling aspect, the length is defined between the axis of the rotor and the vertical axis ( $Z_B$ ),  $l = D/2$ . In this work, conventional configurations are considered, where there is no overlapping of the operating surfaces of the propulsion.

Fig. 26 shows the expected diameters of the multirotor UAV for quadrotor, hexarotor, and octorotor, regarding propeller diameter which is in the range of 17-32". The multirotor propulsion diameters are obtained from the diameter of the propeller expressed in meters and multiplied by coefficients that depend on the number of rotors (for the quad coefficient is 1.8, for hexa 2.4, and for octo 2.9). The outer diameter is equal to the sum of the diameter of the propulsion configuration and the diameter of the propeller  $D_O = D + d$ . When designing the multirotor UAV, constraints regarding multirotor size may be introduced.

**B. HEAVY-LIFT MULTIROTOR UAV TAKE-OFF MASS**

Keeping in mind the limitations in terms of size and energy consumption, the performance of individual setups will be analyzed. During the initial design phase, the thrust-to-mass ratio (TMR) is introduced, establishing a relationship between the multirotor take-off mass ( $m_{ToM}$ ) and the maximum thrust force of the propulsion module in the vertical axis ( $f_{zmax}$ ). Therefore, take-off mass can be determined by the following expression:

$$m_{ToM} \leq \frac{f_{zmax}}{TMR} \tag{6}$$

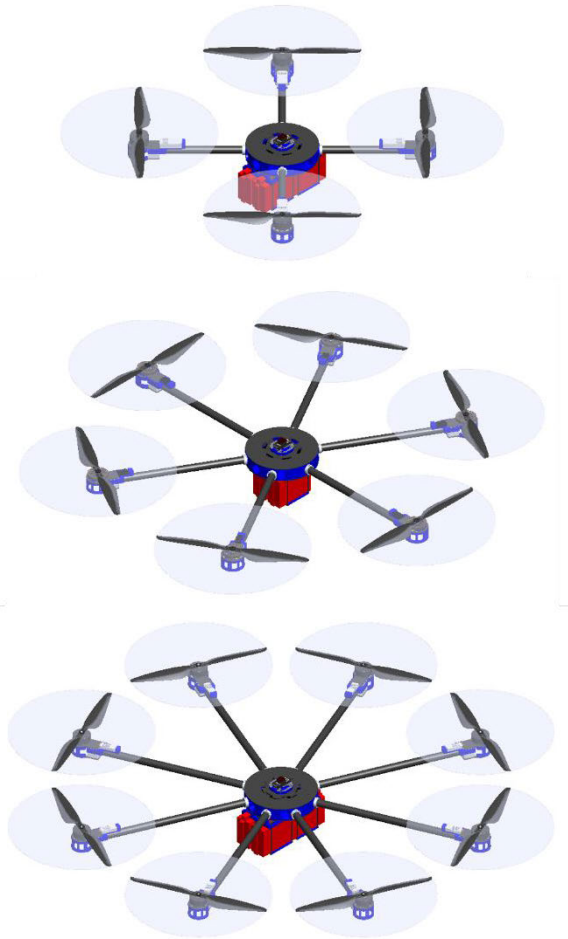


FIGURE 25. Multirotor conventional configurations 3D model.

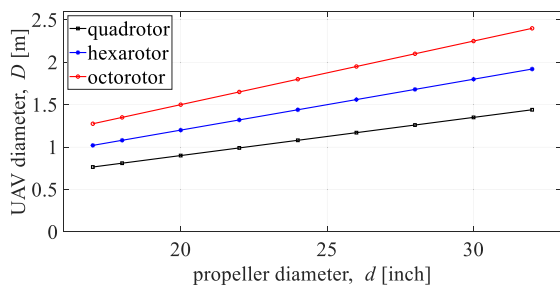


FIGURE 26. The diameter (diagonal) of conventional configurations regarding the propeller diameter and the number of rotors.

In standard terminology, the ratio is often defined as thrust-to weight ratio (TWR), or all up weight (AUW), which is used by the manufacturer of the investigated components.

The motor specifications of the considered setups were searched, and the manufacturer’s recommendations for take-off mass were found for certain setups, with TMR ranging from 1.6 to 3.1, depending on the setup. For example, with the P series motors, for the LV setups (P60 motor), the TMR ranges from 1.6 to 2.7, while for the same series for the HV setups (P80), the TMR is from 2.2 to 2.8. Furthermore, for

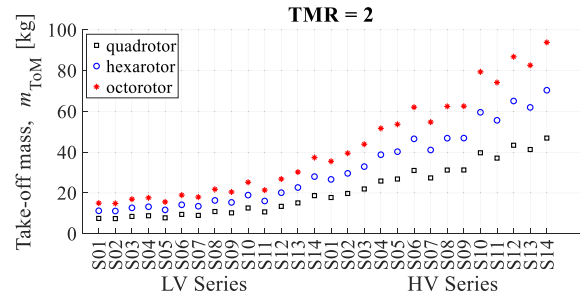


FIGURE 27. Take-off mass of considered setups with regard to assumed TMR.

the Antigravity series of motors, LV setups (MN6007) have a recommended ratio of 2.75, while HV setups (MN1005) have a ratio of 3.1. For the third motor series considered in the research, the U series, only recommendations for smaller motors (U3, U5, and U7) were found, whose ratios range from 1.6 to 2.1.

Through TMR, sufficient agility should be ensured so that the multirotor can take off and can perform the motion in the 3D space required to execute the mission. Furthermore, TMR=2 will be used for both series of EPU setups, and the take-off mass based on the experimental characterization is shown in Fig. 27. The graph shows the values for three configurations where peak thrust is obtained using the second measurement.

### C. HEAVY-LIFT MULTIROTOR UAV ELECTRIC POWER SIZING

The next important aspect of multirotor UAV sizing is regarding the performance in a stationary flight (hovering). Given that in a stationary state, the propulsion configuration should deliver forces that cancel the gravitational force, the electric power for hovering is determined by the overall system mass, which consists of the components, the airframe, and the payload mass. The maximum powers of individual configurations, which are determined by the EPU number and setup, are shown by red bars for LV setups in Fig. 28, while for HV setups are shown in Fig. 29. As with the EPU characterization, peak power is shown for the second measurement. With regard to the presented electric power characteristics as a function of thrust force for LV and HV series (Fig. 13 and 21), it is possible to determine the power for the stationary state.

In this context, the subsequent phase involves determining the energy module parameters, which is accomplished by using a hovering power, which is shown in Fig. 28 and 29 with blue bars. In this segment of sizing, the multirotor battery capacity ( $B_{cap}$ ) is related to hovering power ( $P_{hover}$ ). Regarding the approximation of hover duration ( $t_{hover}$ ) assuming constant voltage and complete discharge, battery capacity can be set

$$B_{cap} \geq \frac{P_{hover}}{u_{bat}} \tilde{t}_{hover}. \quad (7)$$



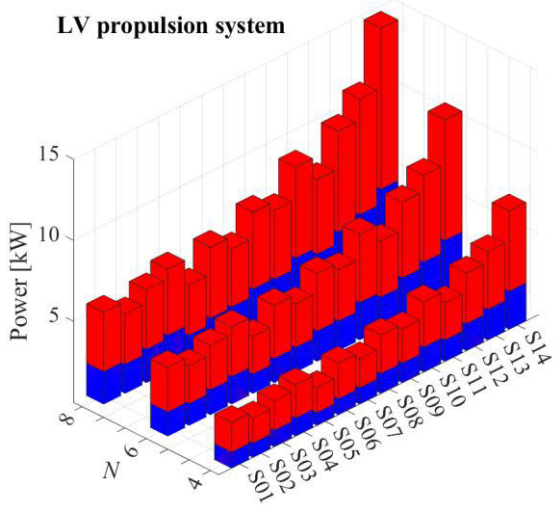


FIGURE 28. Maximum electrical power and hovering power of LV setups.

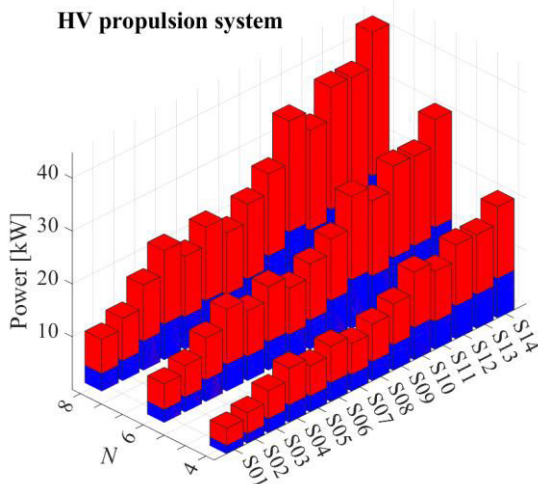


FIGURE 29. Maximum electrical power and hovering power of HV setups.

A hovering time of 30 min is taken as the starting point for further sizing both for the LV and HV series. In a real scenario, the electrical power during the execution of the mission varies depending on the required performance for the mission, and it is a very important fact that it is not recommended to discharge the battery below 3.7 V per cell.

The process of selecting the energy module is incremental, the capacity can be increased with an increase in the number of batteries and with the selection of larger capacity batteries. Consequently, with an increase in the capacity or number of batteries, the mass of the system increases. If there are several batteries in the pack that are connected in parallel, they all must have the same characteristics and parameters. Data is obtained for several manufacturers and different series of 6S (for LV setups) batteries which are shown in Fig. 30, whereas 12S (for HV setups) are shown in Fig. 31. It is important

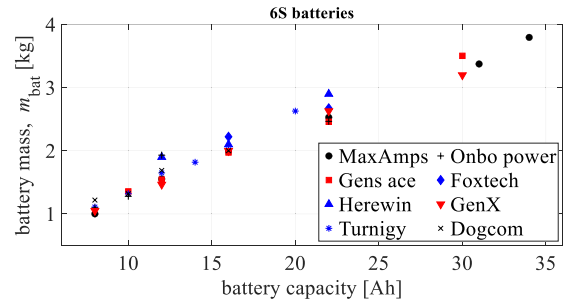


FIGURE 30. Capacity to mass relationship for commercial six-cell (6S) LiPo batteries.

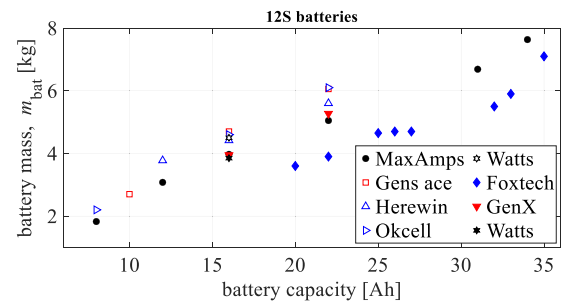


FIGURE 31. Capacity to mass relationship for commercial twelve-cell (12S) LiPo batteries.

to emphasize that the series with non-fill markers include a battery management system (BMS).

#### D. HEAVY-LIFT MULTIROTOR UAV PAYLOAD CAPACITY

Since this paper considers the generic UAV system presented in the previous research [32], the multirotor system can be divided into four key modules whose mass in the design phase is equal to the take-off mass:

$$m_{ToM} = m_{PL} + m_{EM} + m_{PM} + m_{AV}. \quad (8)$$

Given the consideration of a high-payload multirotor, the mass of the control system ( $m_{AV}$ ) is neglected. The mass of the propulsion module ( $m_{PM}$ ) is composed of the rotor arms and the central UAV assembly. The rotor arms consisting of EPU, connections, and airframe parts, are together with other modules connected to the central assembly. The mass of the energy module ( $m_{EM}$ ) is primarily defined by the number and mass of the batteries. When considering the capacity and number of LiPo batteries, it is important to point out that the batteries make up the largest share of the system mass.

To obtain the masses of a generic UAV, apart from the known masses of the components that make up the UAV system, it is necessary to include parts of the airframe in the calculation. For this purpose, the SOLIDWORKS software package is used, in which the airframe parts are 3D modeled. By acquiring a 3D model of UAV assembly, in addition to obtaining mass fractions of modules, moments of inertia are also obtained. Furthermore, the 3D model will be used for the needs of simulations. Based on the first version of the UAV assembly, airframe parts were produced, a quadrotor

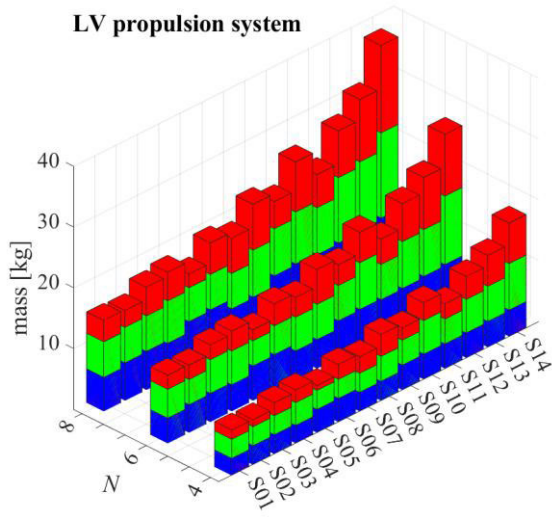


FIGURE 32. System mass distribution for configurations with LV setups.

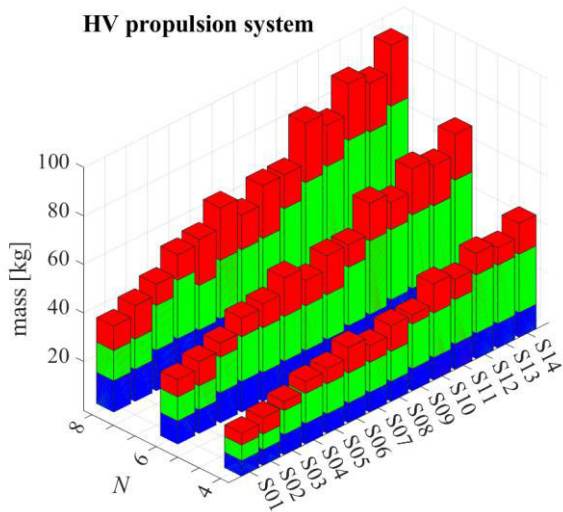


FIGURE 33. System mass distribution for configurations with HV setups.

prototype was assembled and the first tests of the system, shown in previous research, were performed.

Taking into account that introduced TMR and  $\tilde{t}_{\text{hover}}$  can be set, heavy-lift multirotor sizing can be graphically represented with respect to payload capacity ( $m_{\text{PL}}$ ). Fig. 32 shows payload capacities for LV setups, while Fig. 33 shows for HV setups. In both Figures, the mass fraction of the propulsion module is marked in blue, the energy module in green, and the payload capacity in red bar fraction. The graphic display gives a good insight into the possibilities of individual configurations from the aspect of heavy payload missions and can serve as guidance during the design of the multirotor UAV system. By using the presented procedure, it is possible to graphically display the basic performance of a multirotor UAV depending on the ratios on which the dynamics of the UAV and its consumption depend.

TABLE 9. Battery capacity and payload capacity for LV EPU setups.

LV Setup	$N=4$		$N=6$		$N=8$	
	$B_{\text{cap}}$ [Ah]	$m_{\text{PL}}$ [kg]	$B_{\text{cap}}$ [Ah]	$m_{\text{PL}}$ [kg]	$B_{\text{cap}}$ [Ah]	$m_{\text{PL}}$ [kg]
S01	22	1.54	32	2.33	44	3.55
S02	22	1.15	30	2.35	44	2.77
S03	22	2.14	36	3.23	44	4.73
S04	24	2.08	36	3.27	48	4.71
S05	22	0.81	30	1.81	36	2.27
S06	22	2.43	32	3.61	44	5.18
S07	22	2.71	36	4.06	44	5.80
S08	30	3.59	44	5.74	60	7.55
S09	30	2.02	44	3.42	60	4.49
S10	36	2.95	60	5.74	66	8.24
S11	30	2.52	44	4.17	60	5.48
S12	36	3.77	60	6.25	72	7.70
S13	44	5.10	60	8.59	88	10.28
S14	60	6.66	88	10.70	110	14.39

TABLE 10. Battery capacity and payload capacity for HV EPU setups.

HV Setup	$N=4$		$N=6$		$N=8$	
	$B_{\text{cap}}$ [Ah]	$m_{\text{PL}}$ [kg]	$B_{\text{cap}}$ [Ah]	$m_{\text{PL}}$ [kg]	$B_{\text{cap}}$ [Ah]	$m_{\text{PL}}$ [kg]
S01	22	4.83	32	7.11	44	10.07
S02	22	6.70	32	9.89	44	13.74
S03	32	3.65	48	5.78	66	8.71
S04	44	4.89	66	7.62	80	10.47
S05	44	6.37	66	9.81	66	19.02
S06	44	10.46	66	15.91	80	21.44
S07	44	6.79	66	10.45	80	14.20
S08	44	10.54	66	16.03	80	21.61
S09	66	3.72	80	9.20	110	13.89
S10	66	12.04	110	15.40	132	24.49
S11	66	8.27	96	11.27	132	16.94
S12	80	8.80	110	19.01	154	23.31
S13	80	7.14	110	16.55	154	20.06
S14	80	12.65	132	18.81	176	25.03

In Tables 9 and 10, the battery capacities and payload capacities are listed numerically with regard to the considered TMR and  $\tilde{t}_{\text{hover}}$ . Given that the energy module also consists of components used for energy distribution and related sensors, taking into account the available components, the number of LiPo batteries in the package is limited to eight. For the LV propulsion systems, the Gens Ace battery series are discussed, while for the HV propulsion systems, the Herewin battery series. There is a larger selection of commercial 6S batteries, which means that it is possible to fine-tune the system parameters. As a general principle, when the payload mass increases, there is a corresponding increase in the number of rotors and batteries due to the need for additional lift, which can be achieved by adding more rotors and/or increasing motor power. It is evident from the graphs and tables that LV setups are suitable for transporting loads up to 10 kg, except for the octorotor with S14 EPUs, which is

in the range of up to 15 kg, while HV setups are suitable for transporting loads up to 25 kg.

Nevertheless, if shorter missions are considered where smaller battery capacities are needed, therefore the lower mass of the energy module, the payload capacity increases. If, for example, the approximated hovering time is set to 20 minutes, then, a package consisting of five batteries with 22 Ah ( $5 \times 22$ ) is selected for the HV S14 octorotor configuration ( $N = 8$ ), and the payload capacity increases to over 40 kg. Furthermore, if time is further reduced to 15 min, then the same configuration has a payload capacity of up to 50 kg.

It is important to emphasize that when choosing the capacity, the mass of the battery or battery pack is very important. For example, for the LV S12,  $N = 6$ , a  $6 \times 10$  package,  $5 \times 12$  or  $2 \times 30$  package can be used. As expected, the  $2 \times 30$  package has the smallest mass, which, in addition to the need for fewer connectors, sensors, and airframe parts, the ratio between capacity and mass is usually more favorable for larger-capacity batteries. The next important point follows from this fact, which is that it is necessary to consider available combinations, so for example, LV S13,  $N = 8$ , a  $5 \times 16$  package can be used. But the best solution is the  $4 \times 22$  package, which has a higher total capacity and is additionally lighter. A similar example can be mentioned for the HV setup where, for example, for S08,  $N = 6$ , a  $5 \times 12$  package can be used, but it is much more efficient to use a  $3 \times 22$  package, which has 10% more capacity and 10% less mass.

## V. CONCLUSION

This paper presents the characterization and sizing procedure for heavy-lift multirotor UAVs. An experimental approach was used and extensive testing of EPU was carried out (3 measurements per setup, 14 setups per series, two series of setups). By using the framework for data acquisition and processing, the characterization of EPU was enabled based on identified static maps. In the characterization process, a mathematical relation is given for aerodynamic forces and torques and characteristics related to electrical power depending on thrust force. The results for two series of setups (LV and HV) were presented tabularly and graphically. Following the characterization, the sizing procedure for the heavy-lift multirotor UAV was proposed. Multirotor sizes, take-off mass, hovering power, and payload capacity are shown graphically, which systematically provides the insight needed in the design phase of multirotor UAVs. Given that it is a question of heavy payload UAV, the key aspect of sizing is related to payload capacity and potential applications in missions that include the transport of cargo.

The plans for this research include implementing the developed framework as a tool within the methodological design process for multirotor UAVs. In addition, the research will consider the optimization of parameters, taking into account the specific mission requirements and constraints imposed on the multirotor.

## REFERENCES

- [1] Z. Xiong, Y. Xu, Z. Wang, X. Pian, and Y. Wang, "Preliminary design method and prototype testing of a novel rotors retractable hybrid VTOL UAV," *IEEE Access*, vol. 9, pp. 161141–161160, 2021, doi: [10.1109/ACCESS.2021.3131565](https://doi.org/10.1109/ACCESS.2021.3131565).
- [2] E. Gülçh, "Photogrammetric evaluation of multi-temporal fixed wing UAV imagery," *Int. Arch. Photogramm., Remote Sens. Spatial Inf. Sci.*, vol. 38, pp. 265–270, Sep. 2012, doi: [10.5194/isprsarchives-XXXVIII-1-C22-265-2011](https://doi.org/10.5194/isprsarchives-XXXVIII-1-C22-265-2011).
- [3] T. Templin, D. Popielarczyk, and R. Kosecki, "Application of low-cost fixed-wing UAV for inland lakes shoreline investigation," *Pure Appl. Geophys.*, vol. 175, no. 9, pp. 3263–3283, Sep. 2018, doi: [10.1007/s00024-017-1707-7](https://doi.org/10.1007/s00024-017-1707-7).
- [4] *Zipline (Drone Delivery)*. Accessed: Jun. 9, 2023. [Online]. Available: <https://encyclopedia.pub/entry/28276>
- [5] J. Alvarenga, N. I. Vitzilaios, K. P. Valavanis, and M. J. Rutherford, "Survey of unmanned helicopter model-based navigation and control techniques," *J. Intell. Robot. Syst.*, vol. 80, no. 1, pp. 87–138, Oct. 2015, doi: [10.1007/s10846-014-0143-5](https://doi.org/10.1007/s10846-014-0143-5).
- [6] N. P. Nguyen, N. X. Mung, H. L. N. N. Thanh, T. T. Huynh, N. T. Lam, and S. K. Hong, "Adaptive sliding mode control for attitude and altitude system of a quadcopter UAV via neural network," *IEEE Access*, vol. 9, pp. 40076–40085, 2021, doi: [10.1109/ACCESS.2021.3064883](https://doi.org/10.1109/ACCESS.2021.3064883).
- [7] G. Ducard and M.-D. Hua, "WCA: A new efficient nonlinear adaptive control allocation for planar hexacopters," *IEEE Access*, vol. 11, pp. 37714–37748, 2023, doi: [10.1109/ACCESS.2023.3261240](https://doi.org/10.1109/ACCESS.2023.3261240).
- [8] D. Bicego, J. Mazzetto, R. Carli, M. Farina, and A. Franchi, "Nonlinear model predictive control with enhanced actuator model for multi-rotor aerial vehicles with generic designs," *J. Intell. Robot. Syst.*, vol. 100, nos. 3–4, pp. 1213–1247, Dec. 2020, doi: [10.1007/s10846-020-01250-9](https://doi.org/10.1007/s10846-020-01250-9).
- [9] K. Klausen, T. I. Fossen, T. A. Johansen, and A. P. Aguiar, "Cooperative path-following for multirotor UAVs with a suspended payload," in *Proc. IEEE Conf. Control Appl. (CCA)*, Sep. 2015, pp. 1354–1360, doi: [10.1109/CCA.2015.7320800](https://doi.org/10.1109/CCA.2015.7320800).
- [10] K. Dorling, J. Heinrichs, G. G. Messier, and S. Magierowski, "Vehicle routing problems for drone delivery," *IEEE Trans. Syst., Man, Cybern., Syst.*, vol. 47, no. 1, pp. 70–85, Jan. 2017, doi: [10.1109/TSMC.2016.2582745](https://doi.org/10.1109/TSMC.2016.2582745).
- [11] M. Orsag, C. Korpela, S. Bogdan, and P. Oh, "Dexterous aerial robots—Mobile manipulation using unmanned aerial systems," *IEEE Trans. Robot.*, vol. 33, no. 6, pp. 1453–1466, Dec. 2017, doi: [10.1109/TRO.2017.2750693](https://doi.org/10.1109/TRO.2017.2750693).
- [12] M. Ryll, G. Muscio, F. Pierri, E. Cataldi, G. Antonelli, F. Caccavale, D. Bicego, and A. Franchi, "6D interaction control with aerial robots: The flying end-effector paradigm," *Int. J. Robot. Res.*, vol. 38, no. 9, pp. 1045–1062, Aug. 2019, doi: [10.1177/0278364919856694](https://doi.org/10.1177/0278364919856694).
- [13] B. J. Brelje and J. R. Martins, "Electric, hybrid, and turboelectric fixed-wing aircraft: A review of concepts, models, and design approaches," *Prog. Aerosp. Sci.*, vol. 104, pp. 1–19, Jan. 2019, doi: [0.1016/j.paerosci.2018.06.004](https://doi.org/10.1016/j.paerosci.2018.06.004).
- [14] E. Saif and I. Eminoglu, "Hybrid power systems in multi-rotor UAVs: A scientific research and industrial production perspective," *IEEE Access*, vol. 11, pp. 438–458, 2023, doi: [10.1109/ACCESS.2022.3232958](https://doi.org/10.1109/ACCESS.2022.3232958).
- [15] M. Krznar, P. Piljek, D. Kotarski, and D. Pavković, "Modeling, control system design and preliminary experimental verification of a hybrid power unit suitable for multirotor UAVs," *Energies*, vol. 14, no. 9, p. 2669, May 2021, doi: [10.3390/en14092669](https://doi.org/10.3390/en14092669).
- [16] C. Depcik, T. Cassady, B. Collicott, S. P. Burugupally, X. Li, S. S. Alam, J. R. Arandia, and J. Hobeck, "Comparison of lithium ion batteries, hydrogen fueled combustion engines, and a hydrogen fuel cell in powering a small unmanned aerial vehicle," *Energy Convers. Manag.*, vol. 207, Mar. 2020, Art. no. 112514, doi: [10.1016/j.enconman.2020.112514](https://doi.org/10.1016/j.enconman.2020.112514).
- [17] J. Apeland, D. Pavlou, and T. Hemmingsen, "State-of-technology and barriers for adoption of fuel cell powered multirotor drones," in *Proc. Int. Conf. Unmanned Aircr. Syst. (ICUAS)*, Sep. 2020, pp. 1359–1367, doi: [10.1109/ICUAS48674.2020.9213971](https://doi.org/10.1109/ICUAS48674.2020.9213971).
- [18] D. Bershadsky, S. Haviland, and E. N. Johnson, "Electric multirotor UAV propulsion system sizing for performance prediction and design optimization," in *Proc. 57th AIAA/ASCE/AHS/ASC Struct., Structural Dyn., Mater. Conf.*, San Diego, CA, USA, Jan. 2016, pp. 4–8, doi: [10.2514/6.2016-0581](https://doi.org/10.2514/6.2016-0581).



- [19] A. S. Prasetya, R.-J. Wai, Y.-L. Wen, and Y.-K. Wang, "Mission-based energy consumption prediction of multirotor UAV," *IEEE Access*, vol. 7, pp. 33055–33063, 2019, doi: [10.1109/ACCESS.2019.2903644](https://doi.org/10.1109/ACCESS.2019.2903644).
- [20] M. Biczyski, R. Sehab, J. F. Whidborne, G. Krebs, and P. Luk, "Multirotor sizing methodology with flight time estimation," *J. Adv. Transp.*, vol. 2020, pp. 1–14, Jan. 2020, doi: [10.1155/2020/9689604](https://doi.org/10.1155/2020/9689604).
- [21] S. Chahba, R. Sehab, C. Morel, G. Krebs, and A. Akrad, "Fast sizing methodology and assessment of energy storage configuration on the flight time of a multirotor aerial vehicle," *Aerospace*, vol. 10, no. 5, p. 425, Apr. 2023, doi: [10.3390/aerospace10050425](https://doi.org/10.3390/aerospace10050425).
- [22] E. L. de Angelis, F. Giuliotti, G. Rossetti, and G. Bellani, "Performance analysis and optimal sizing of electric multirotors," *Aerosp. Sci. Technol.*, vol. 118, Nov. 2021, Art. no. 107057, doi: [10.1016/j.ast.2021.107057](https://doi.org/10.1016/j.ast.2021.107057).
- [23] M. Budinger, A. Reysset, A. Ochotorena, and S. Delbecq, "Scaling laws and similarity models for the preliminary design of multirotor drones," *Aerosp. Sci. Technol.*, vol. 98, Mar. 2020, Art. no. 105658, doi: [10.1016/j.ast.2019.105658](https://doi.org/10.1016/j.ast.2019.105658).
- [24] S. Delbecq, M. Budinger, A. Ochotorena, A. Reysset, and F. Defay, "Efficient sizing and optimization of multirotor drones based on scaling laws and similarity models," *Aerosp. Sci. Technol.*, vol. 102, Jul. 2020, Art. no. 105873, doi: [10.1016/j.ast.2020.105873](https://doi.org/10.1016/j.ast.2020.105873).
- [25] J. Buzzatto and M. Liarokapis, "A benchmarking platform and a control allocation method for improving the efficiency of coaxial rotor systems," *IEEE Robot. Autom. Lett.*, vol. 7, no. 2, pp. 5302–5309, Apr. 2022, doi: [10.1109/LRA.2022.3153999](https://doi.org/10.1109/LRA.2022.3153999).
- [26] W. Ong, S. Srigrarom, and H. Hesse, "Design methodology for heavy-lift unmanned aerial vehicles with coaxial rotors," in *Proc. AIAA Scitech Forum*, San Diego, CA, USA, Jan. 2019, pp. 7–11, doi: [10.2514/6.2019-2095](https://doi.org/10.2514/6.2019-2095).
- [27] A. B. Weishäupl and S. D. Prior, "Influence of propeller overlap on large-scale tandem UAV performance," *Unmanned Syst.*, vol. 7, no. 4, pp. 245–260, Oct. 2019, doi: [10.1142/S2301385019500092](https://doi.org/10.1142/S2301385019500092).
- [28] J. Jeong, H. Shi, K. Lee, and B. Kang, "Improvement of electric propulsion system model for performance analysis of large-size multicopter UAVs," *Appl. Sci.*, vol. 10, no. 22, p. 8080, Nov. 2020, doi: [10.3390/app10228080](https://doi.org/10.3390/app10228080).
- [29] N. A. Vu, D. K. Dang, and T. Le Dinh, "Electric propulsion system sizing methodology for an agriculture multicopter," *Aerosp. Sci. Technol.*, vol. 90, pp. 314–326, Jul. 2019, doi: [10.1016/j.ast.2019.04.044](https://doi.org/10.1016/j.ast.2019.04.044).
- [30] M. D. Ardem, *Newton-Euler Dynamics*, 1st ed. New York, NY, USA: Springer, 2006.
- [31] T. I. Fossen, *Guidance and Control of Ocean Vehicles*, 1st ed. Chichester, U.K.: Wiley, 1994.
- [32] D. Kotarski, P. Piljek, M. Pranjić, and J. Kasać, "Concept of a modular multirotor heavy lift unmanned aerial vehicle platform," *Aerospace*, vol. 10, no. 6, p. 528, Jun. 2023, doi: [10.3390/aerospace10060528](https://doi.org/10.3390/aerospace10060528).
- [33] *Series 1780 Test Stand Datasheet*. Accessed: Jun. 12, 2023. [Online]. Available: [https://cdn.rcbenchmark.com/landing\\_pages/Manuals/Series%201780%20Datasheet.pdf](https://cdn.rcbenchmark.com/landing_pages/Manuals/Series%201780%20Datasheet.pdf)



**PETAR PILJEK** received the B.S.M.E., M.S.M.E., and Ph.D. degrees in mechanical engineering from the Faculty of Mechanical Engineering and Naval Architecture, University of Zagreb (UNIZG), in 2009, 2010, and 2017, respectively.

He is currently an Assistant Professor with the Department of Technology, Faculty of Mechanical Engineering and Naval Architecture, UNIZG. As a Researcher, he participated in several projects of the Ministry of Science, Education, and Sport, Republic of Croatia, and projects supported by UNIZG. He is also a Researcher in EU projects: "Strengthening Research and Innovation Excellence in Autonomous Aerial Systems – AeroSTREAM" and "Research and Development of Specialised Multirotor Unmanned Aerial Vehicles." He has published more than 40 scientific publications in the field of unmanned aerial systems, robotics, and mechanical technologies. His research interests include mechanical technologies, additive manufacturing, robotics, and multirotor UAVs.



**DENIS KOTARSKI** received the B.S.M.E., M.S.M.E., and Ph.D. degrees in mechanical engineering from the Faculty of Mechanical Engineering and Naval Architecture, University of Zagreb (UNIZG), in 2010, 2011, and 2020, respectively.

He is currently with the Department of Mechanical Engineering, Karlovac University of Applied Sciences. As a Researcher, he participated in several national and international research projects in the field of robotics and unmanned aerial vehicles.

He is also a Researcher in EU projects: "Research and Development of Specialised Multirotor Unmanned Aerial Vehicles" and "Strengthening Research and Innovation Excellence in Autonomous Aerial Systems – AeroSTREAM." He has authored and coauthored more than 30 scientific and professional papers, including journals and conference papers, and book chapters in the field of unmanned aerial systems and robotics. His research interests include multirotor UAVs, robotics, and mechatronics system design.



**JOSIP KASAĆ** received the graduate degree in physics from the Faculty of Science, University of Zagreb, in 1995, and the Ph.D. degree in mechanical engineering from the Faculty of Mechanical Engineering and Naval Architecture, University of Zagreb, in 2005.

He is currently a Full Professor with the Department of Robotics and Automation of Manufacturing Systems, Faculty of Mechanical Engineering and Naval Architecture, University of Zagreb. As a Researcher, he participated in several projects of the Government of the Republic of Croatia, projects supported by the University of Zagreb, Horizon, and EU-funded projects. He is also working on an EU Project: "Strengthening Research and Innovation Excellence in Autonomous Aerial Systems – AeroSTREAM." His research interests include the control of nonlinear mechanical systems, optimal control and algebraic estimation methods, and multirotor UAVs.

...